Science and Technology Publishing (SCI & TECH)
ISSN: 2632-1017
Vol. 8 Issue 7, July - 2024

Accuracies of k-ε Models and Simulation of Viscous Flow over Two Circular Cylinders

Rahaman Abu
Department of Mechanical Engineering
University of Ibadan
Ibadan, Nigeria
aburahaman@yahoo.com

Kareem Abu
Department of Mechanical Engineering
University of Ibadan
Ibadan, Nigeria
abukareemid@yahoo.com

Abstract*— Viscous flow over cylinders exhibits turbulence which can be modeled by numerous turbulence models. The accuracies of the RNG k-ε, standard k-ε, realizable k-ε models over a single cylinder were compared using the commercial finite volume method codes of ANSYS Fluent. When these three models were compared with LES and experimental data, the RNG k- model produced the most precise results. It was thus extended to the investigation of vortex shedding, lift coefficient (Cl), Strouhal number (St) and drag coefficient (Cd) over a pair of circular cylinders that were side by side at the Reynolds number Re = 1500 at the spacing ratios (g/D) of 1.75, 2.00, 2.50, 3.00, 3.50, 4.00 and 5.00. The vortex shedding behind the cylinders was influenced by biased flow occurring at small gaps g/D ≤ 2.0; and exhibited anti-phase or in-phase pattern at g/D ≥ 2.5, with flow interference diminishing as g/D increases. The biased flow also influenced the pattern of Cd and Cl fluctuations over the cylinders at these small gaps, as well as St so that two peaks were recorded in the power spectral density for both cylinders. The mean lift coefficients $\bar{Cl}$ of the upper cylinder were highest at these small gaps. Except at g/D=2.50, the upper cylinder had $\bar{Cl}$ values that were greater than values of the lower cylinder. This study suggests that among the three models considered, the RNG k-turbulence model provides the most precise result for viscous flows over cylinders.

Keywords*— k-ε turbulence model; lift coefficient; drag coefficient; vortex shedding; biased flow; side-by-side

I. Introduction

Fluid dynamic problems involving turbulence are usually represented by Navier-Stokes equations. Different turbulence models have been developed to solve these equations. Three of such models are the renormalization group (RNG), standard and realizable k-ε turbulence models. They are popular turbulent models for solution of flow and/or heat transfer problems. For instance, Oyewola *et al.* adopted the standard k-ε turbulence model to determine the coefficients of drag and lift as well as the heat characteristics over two tandem circular cylinders, using finite element method [1, 2]. On accuracy basis, it had been shown that RNG k-ε model yielded better prediction than standard k-ε model for flows with high strains, swirl and separation [3]. Furthermore, it was shown to be suitable for high Reynolds-number (Re) flow, low Reynolds-number flow and near-wall effect. Similarly, Shih *et al*. specifically presented realizable k-ε as an advancement on standard k-ε model so that it was suitable for flows concerning rotation, planar and round jets, or adverse pressure gradient [4]. The RNG models and realizable k-ε are advancements on the standard k-ε model, and are both suitable for simulating flow over bluff bodies.

Consequently, different authors have assessed the accuracy of these turbulence models. Chen-Kim k-ε, standard k-ε and RNG k-ε turbulence models were compared, and it was deduced that the first two models gave much better prediction of structure of the flow separation and vortex than the last turbulence model [5]. Wang developed a high-resolution total variation diminishing (TVD) finite-volume scheme, using the RNG k-ε turbulence model, to solve a single-cylinder flow at Re = 1000 and 3900 [6]. The work reported that, given the accuracy achievable by RNG k-ε and the relatively less computation time, RNG k-ε was as reliable as the results of large eddy simulation (LES) and direct numerical simulation (DNS) which have greater computational cost. Similarly, among k-ε turbulence models evaluated at Re = 21400 for flow over a square cylinder, the realizable k-ε yielded coefficients of drags and lift approximately closest to experimental results and LES results [7]. However, realizable k-ε model seemed to have over forecast the Strouhal number (St) in the work. In a flow simulation around a building, the three k-ε turbulence models were demonstrated to produced nearly the same air velocity flow around a building [8]. They also reported that the realizable k-ε and standard k-ε models appeared to produce similar recirculation zones, but the RNG k-ε model significantly overpredicted the recirculation zone. Between the three models, the RNG k-ε model yielded the pressure coefficient closest to the stipulated 0.8 pressure coefficient value of the Myanmar National Building Code.

In the like manner, eight different Reynolds-averaged Navier-Stokes (RANS) two-equation turbulence models were compared in the study of three-dimensional flow over a circular cylinder at Re = 20 000 [9]. Based on the fact that LES models provide quasi exact solution, the outputs of the eight RANS models were compared with the Smagorinsky LES model. Between the three k-ε models, the realizable k-

ε offered coefficient of drag value closest to the LES results. Also, the predictive ability of these three k-ε models in the examination of flow around a bluff body had been compared by Pang et al [10]. As for the k-ε models considered in the work, RNG k-ε model yielded Strouhal number and rms lift coefficient which agreed satisfactorily with the available experimental data; the realizable k-ε and standard k-ε model models underpredicted the rms lift coefficient and overpredicted Strouhal number. In another study, the RNG k-ε model and standard k-ε model appeared to have underpredicted the coefficient of drag, while realizable k-ε model gave drag coefficient value very close to the experimental result [11]. From the foregoing discussion, it can be inferred that when modeling a certain problem with the k-ε turbulence models, it is important to identify which of the models optimally predicts a parameter being considered. In Fluent Theory Guide, it is suggested that realizable k-ε is the most accurate of all k-ε models [12]. However, no clear-cut assertions were given, as to nature and types of problems for which it was most accurate, so as to establish the superiority of realizable k-ε over RNG k-ε model.

It is therefore necessary to evaluate the accuracy of these three turbulence models to be able to make a choice of the model to use for prediction of a particular parameter. This present work applied standard k-ε, RNG k-ε and realizable k-ε turbulence models to one circular cylinder and then compared the results with those of literature to determine which model best optimized drag and coefficients of lift along with Strouhal number. These were carried out at Re = 300, 1000 and 3900. Furthermore, and by extension, simulations were conducted at Re = 1500 for flows over two cylinders arranged side by side, using the model with relatively better accuracy as determined. At this Reynolds number, spacing (centre-to-centre spacing) ratios g/D = 1.75, 2.00, 2.50, 3.00, 3.50, 4.00 and 5.00 were considered. The coefficients of lift, coefficient of drag, Strouhal number as well as vortex shedding were determined and presented.

II. Governing Differential Equations

The governing differential equations of incompressible flow and RNG turbulence model have been well presented [13]. The reason for the choice of this model was discussed in the validation section of this paper. The ANSYS Fluent commercial codes were used to find solution to the governing equations with the suitable boundary conditions as shown in Fig. 1. The continuity equation (Equation (1)) and represents the momentum equations (Equation (2)) are with *i* = 1, 2 for two-dimensional flow.

$$\frac{\partial u_i}{\partial x_i} = 0 \tag{1}$$

$$\frac{\partial u_i}{\partial t} + \frac{\partial}{\partial x_j}\left(u_i u_j\right) = -\frac{1}{\rho}\frac{\partial p}{\partial x_i} + \frac{\partial}{\partial x_j}\left(\frac{\mu}{\rho}\frac{\partial u_i}{\partial x_i}\right) + \frac{1}{\rho}\frac{\partial}{\partial x_j}\left(-\rho\overline{u_i u_j}\right) \tag{2}$$

where $\rho u_i u_j$ is the Reynolds stress. Equation (3) defines the Reynolds stress.

$$\tau_{ij} = -\rho\overline{u_i u_j} = -\frac{2}{3}\rho k\delta_{ij} + \mu_t\left(\frac{\partial u_i}{\partial x_j} + \frac{\partial u_j}{\partial x_i}\right) \tag{3}$$

where $\delta_{ij} = \begin{cases} 1, i = j \\ 0, i \neq j \end{cases}$ and

$$\mu_t = \rho C_\mu \frac{k^2}{\varepsilon} \tag{4}$$

For incompressible flow, the RNG k-ε turbulence model is characterized with Equations (5) and (6) [12].

$$\frac{\partial(\rho k)}{\partial t} + \frac{\partial}{\partial x_j}\left(\rho k u_j\right) = \frac{\partial}{\partial x_j}\left[\alpha_k\left(\mu + \mu_t\right)\frac{\partial k}{\partial x_j}\right] + \tau_{ij}\cdot S_{ij} - \rho\varepsilon \tag{5}$$

$$\frac{\partial(\rho\varepsilon)}{\partial t} + \frac{\partial}{\partial x_j}\left(\rho\varepsilon u_j\right) = \frac{\partial}{\partial x_j}\left[\alpha_\varepsilon\left(\mu + \mu_t\right)\frac{\partial \varepsilon}{\partial x_j}\right] + C_{1\varepsilon}^{*}\frac{\varepsilon}{k}\cdot S_{ij} - C_{2\varepsilon}\rho\frac{\varepsilon^2}{k} \tag{6}$$

where

$$S_{ij} = \frac{1}{2}\left(\frac{\partial u_i}{\partial x_i} + \frac{\partial u_j}{\partial x_i}\right) \tag{7}$$

$\alpha_k = \alpha_\varepsilon = 1.39$; i, j = 1, 2; $C_{1\epsilon} = 1.42$, $C_{2\epsilon} = 1.68$, $C_\mu = 0.0845$. μ_t is turbulence dynamic viscosity; μ is molecular dynamic viscosity. The over-bar symbol over some variable indicates average value. S_{ij} is defined as the rate of deformation. $C^{*}_{1\varepsilon}$ present in Equation (6) is defined by Equation (8).

$$C_{1\varepsilon}^{*} = C_{1\varepsilon} - \frac{\eta\left(1 - \frac{\eta}{\eta_0}\right)}{1 + \beta\eta^3} \tag{8}$$

where

$$\eta = \frac{k}{\varepsilon}\sqrt{2S_{ij}.S_{ij}}\ ;\ \eta_0 = 4.377; \beta = 0.012 \tag{9}$$

in which ε is rate of dissipation of the energy and *k* is rate of production of turbulent kinetic energy.

As for the fluctuating forces, the coefficient of drag C_D and coefficient of lift C_L are expressed by equations 10 and 11. The drag and lift forces are denoted by F_D and F_L, respectively.

$$C_D = \frac{F_D}{0.5\rho U_\infty^2 D} \tag{10}$$

$$C_L = \frac{F_L}{0.5\rho U_\infty^2 D} \tag{11}$$

These governing equations were solved using ANSYS FLUENT commercial codes. Velocity and pressure were integrated using the SIMPLE algorithm. For the spatial discretization of pressure, the second-order was utilized. For the time domain, the second-order implicit transient formulation was

applied, and the momentum, turbulence kinetic energy and turbulence dissipation rates were determined employing the second-order upwind scheme. These schemes have been detailed elsewhere [13] and provided in ANSYS FLUENT.

III. Computational Domain

Fig. 1 depicts the flow domain and two adjacent cylinders within the domain. The pair of cylinders are arranged and spaced about the horizontal line of symmetry. They were located 10D from the outlet and 13D from the inlet, where D is the diameter of the cylinders and g is the space between the cylinders. The cylinders were thus positioned within the domain to minimize the inlet and outlet effects. The centers of the upper and lower cylinders were located respectively ≥ 5D from the upper and lower boundaries of the domain. 5D was enough to minimize the proximity effects [14]. The configuration and dimension were chosen based on the experimental finding which showed that mean drag coefficient had no significant variation with blockage ratio within 9-15% [15]; the blockage ratio in this study is 13%.

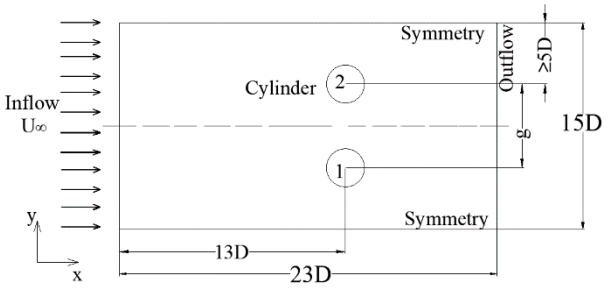

Fig. 1. Problem geometry and boundary conditions. Only g/D is used to obtain critical spacing ratio

Inflow boundary condition was adopted at the inlet, outflow boundary condition at the outlet, and symmetry boundary condition at the upper and lower boundaries of the domain. The cylinder surface was subjected to the no-slip boundary condition. To achieve the near-wall effect, the standard wall function was employed [16]. The boundary conditions were defined as follows.

Inflow boundary: $u = U_\infty$, $v = 0$; U_∞ is free stream velocity.

Outflow boundary: $\frac{\partial u}{\partial x} = 0, \frac{\partial v}{\partial x} = 0$.

Symmetry: $v = 0; \frac{\partial u}{\partial y} = 0$.

No-slip: $u = u_{wall} = 0$ (at the cylinder surface).

IV. Validation

Simulations were conducted at Re =300, 1000 and 3900 over a single cylinder. At each of the Re, the maximum coefficient of lift (Cl) and mean coefficient of drag (Cd) values were generated. Standard k-ε, RNG k-ε and realizable k-ε models were compared in Table I at Re =300. It was deduced from Table I that RNG k-ε closely forecasted the average of Cd values presented by [17-19], while standard k-ε predicted Cd above the average, and realizable k-ε underpredicted the average.

TABLE I. COMPARISON OF CD OVER A SINGLE CYLINDER OBTAINED USING THREE K-E MODELS AT RE =300

Present		Lima E Silva et al. [17]	Park et al [18]	Sucker and Brauer [19]
Standard k-ε	1.35	1.27	1.37	1.22
RNG k-ε	1.22			
Realizable k-ε	1.14			

At Reynolds number Re =1000, it can be deduced from Table II that all three models well predicted drag coefficient over the cylinder. However, the standard k-ε appeared to have the best drag coefficient prediction compared with the results obtained by LES 3-D [20], curvilinear coordinate Laminar 2D method [21] and experiment [22]. As for lift coefficient prediction, RNG k-ε yielded Cl of 0.47 which is a value in-between those of Huang et al [21] and TVD-finite volume method [6]. It also gave St which was close to the one presented by Roshko [22]. The standard and realizable k-ε models greatly underpredicted the lift coefficient. Though the realizable k-ε model yielded least forecasted Cd and Cl of the three k-ε models, it forecasted the St closely.

At Re =3900, it was also clear that that RNG k-ε yielded altogether values of Cd and Cl closest to the results of LES, 3D [23], LES,3D [24] and experiment [25]. Consequently, RNG predicted the Cd, Cl and St fairly better than the other two models for the two Reynolds number (i.e., Re = 1000 and Re = 3900) considered.

Therefore, RNG k-ε model was chosen as the turbulence model for the flow over a pair of circular cylinders at Re =1500. This Reynolds number was chosen as it falls within 1000≤Re≤3900, and to ensure that results obtained are within the limits of validation.

TABLE II. COMPARISON OF STANDARD, RNG AND REALIZABLE K-E MODELS OVER SINGLE CYLINDER

Re	Method		Cd	Cl	St
1000	LES,3-D [20]		1.2	0.72	0.215
	Curvilinear coordinate, laminar, 2-D [21]		1.2	0.40	0.216
	Experiment [22]		1.2	-	0.210
	TVD-finite volume method (FVM) [6]		1.14	0.54	0.191
	Present	Standard k-ε	1.14	0.345	0.193
		RNG k-ε	1.12	0.465	0.199
		Realizable k-ε	1.04	0.336	0.200
3900	LES,3-D [23]		1.04	-	0.210
	LES,3-D [24]		1.2	0.5	0.216
	Experiment [25]		0.99	-	0.215
	TVD-FVM [6]		1.06	0.6	0.196
	Present	Standard k-ε	0.92	0.3	0.192
		RNG k-ε	0.85	0.4	0.201
		Realizable k-ε	0.90	0.3	0.202

Analyzing the drag coefficient and lift coefficient converged history data, it was clear that the Cd and Cl are respectively the average and maximum of the entire converged solutions when compared with data available from the literature. Cd and Cl are presented in Tables I - IV refer to these meanings.

Fig. 2 shows a typical vortex shedding common to the flow over a cylinder at the Reynolds numbers Re =300, 1000 and 3900 considered in the validation procedure.

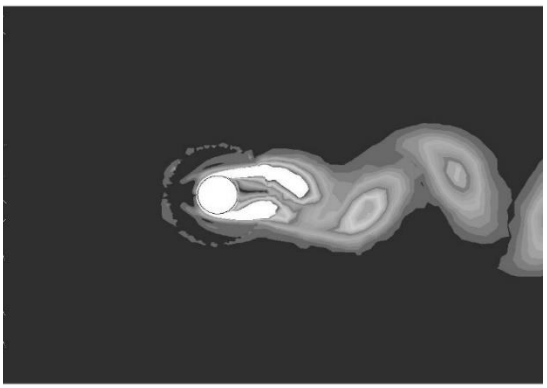

Fig. 2. Vortex shedding behind a cylinder that is typical of Re = 300, 1000 and 3900.

V. MESH DEPENDENCE

Numerical solution involves dividing problem geometry into small grids, all together referred to as mesh. The discretized governing differential equations are then applied to each of the grids making up the mesh, to evaluate values of different flow parameters at the nodes. Generally, the finer the mesh the better the result obtained. However, when it is apparent that using much smaller nodes does not appreciably improve or change the result, the solution is said to be mesh-independent.

Fig. 3 depicts linear-order triangular meshing throughout the flow domain, with the mesh being particularly finer (element size = 1mm) around the cylinder within the rectangular domain of global element size of 0.3 m. The parameters of interest for investigation includes lift coefficient, drag coefficient and Strouhal number were evaluated around the cylinder. This explains the reason why more grids and fine mesh are required at the cylinder surface.

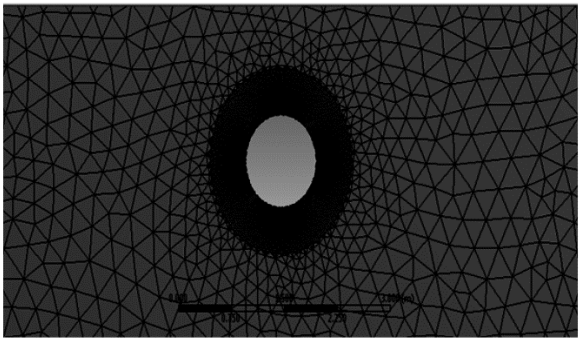

Fig. 3. Fine mesh surrounding the cylinder- the mesh is denser around the cylinder because Cd, Cl and St are calculated around it.

Three different mesh sizes with RNG turbulence model were used differently to determine the Cd and Cl over the single cylinder at Re=1000. For the purpose of nomenclature, these mesh sizes were tagged A, B, and C. A had 30 inflation layers, 10772 nodes and 13543 elements; B had 40 inflation layers, 13144 nodes and 15777 elements; and C had 50 inflation layers, 15558 nodes and 18095 elements. All layers grew at the rate of 2.5 and had first-layer-thickness height of 1 mm. Table III compares the results obtained for the three mesh sizes over a single cylinder.

The number of elements decreases from meshes C through B to A. The Cd value is independent of the mesh elements. However, comparing B with C, difference in Cl value is 2.5%, while comparing A with B, difference in Cl value is 2.2%. Therefore, it is concluded that Cd and Cl are independent of the mesh sizes. These values agree with Wang [5]. So, inflation layer definition for mesh B was adopted for single-cylinder simulations.

TABLE III. CHECKING FOR MESH INDPENDENCE- The mesh labelled B, with intermediate number of elements, depicts the mesh independence and was adopted for the single-cylinder case. Re =1000.

	A	B	C
Cd	1.12	1.12	1.12
Cl	0.475	0.465	0.477

In a computational domain, where two cylinders are involved, the meshes around the cylinders must be carefully created so that those of one cylinder do not overlap those of the other cylinder. Moreover, these meshes are primarily created such that the minimum orthogonal quality exceeds 0.5. While in the single cylinder, simulation results appeared not to depend on the number of inflation layers, inflation layers of about 20 tended to overlap the adjacent cylinder for two side-by-side cylinders consideration. To avoid mesh overlap, the smaller inflation of layers 5 and 10 for double cylinders at Re =1000 was tested. The lower and upper cylinders respectively had mean Cd of 1.11 and 1.12 with 5 inflation layers, while they have Cd of 1.23 and 1.19 for 10 layers at a spacing g/D of 2.0. These values fall within the range of average coefficient of drag obtainable over a cylinder as shown in Table II. Therefore, inflation layers of 10 growing at the rate of 2.5 was used for all the spacing ratios in the double-cylinder simulations while ensuring that minimum orthogonality quality was greater 0.5.

VI. Results- Two Cylinders

A. Vortex Shedding behind the Cylinders

The vortex structure helps to show vortices as they are being shed from the cylinders. It shows how vortices shed from one cylinder deflect or move towards the other cylinder in the phenomenon known as biased flow. Fig. 4 illustrates the biased flow at g/D = 1.75 and 2.00. Fig. 4a shows the vortices from the upper part of the lower cylinder merging with the vortices shed from the upper cylinder due to biased flow. Fig. 4b shows that lower vortices from the lower cylinder tended upwards to that of the upper cylinder. This accounts for the irregular fluctuation observed in the drag and lift coefficients at the g/D ratio. In addition, the biased flow contributes to the increase in the lift coefficients and Strouhal number at these small gap ratios as discussed in section VI.C.

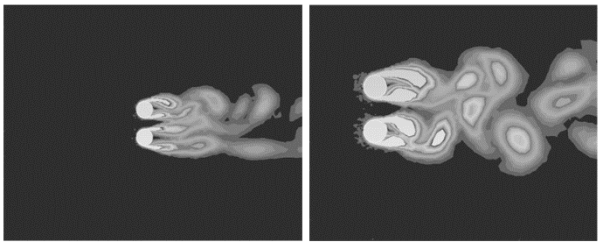

(a) (b)

Fig. 4. Vortex shedding at (a) g/D = 1.75; (b) g/D =2.00, both at Re = 1500. In each case, vortices downstream merged due to biased flow

The vortex shedding behind the cylinders become distinct at g/D ≥ 3.50. At g/D = 5.00, the vortex shedding behind both cylinders were clearly apart from each other, so that the flow interference at higher g/D (i.e., g/D = 3.50, 4.00 and 5.00) was greatly reduced (Fig. 5). At these g/D, anti-phase synchronized vortex shedding occurred (Fig. 5). However, at 2.50≤g/D≤3.00, the in-phase vortex shedding behind the cylinders combined downstream (Fig. 6).

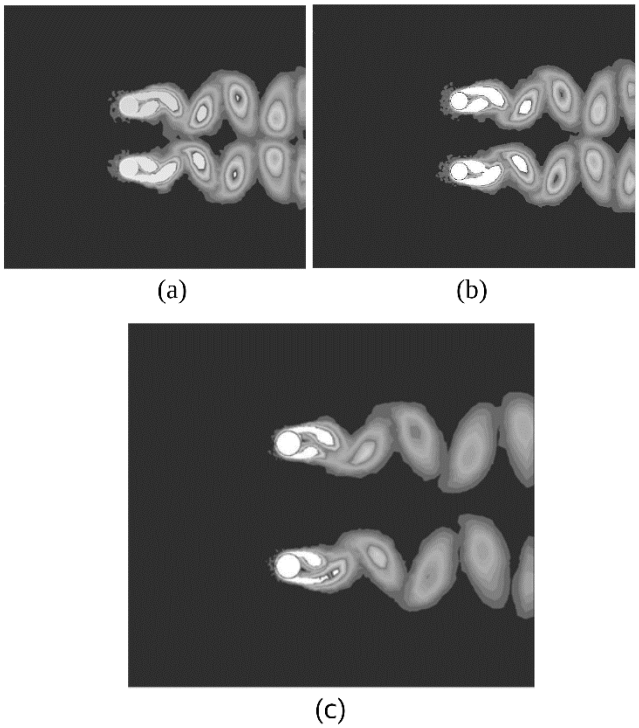

(a) (b)

(c)

Fig. 5. Vortex shedding behind two cylinders at: (a) g/D =3.50; (b) g/D =4.00, and (c) g/d = 5.00 Vortices shed from the two cylinders are in anti-phase, and interference between them was highly diminished at g/D = 3.50, 4.00 but absent at gd = 5.00.

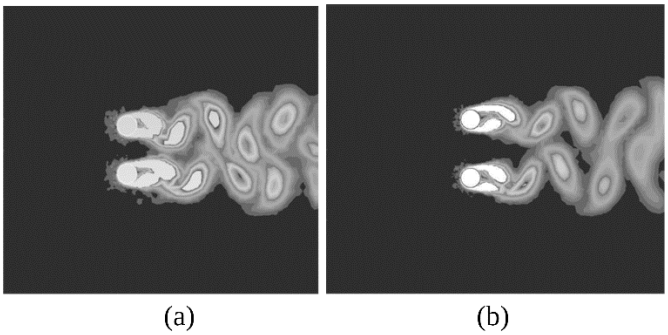

(a) (b)

Fig. 6. Vortex shedding behind two cylinders: (a) at g/D =2.50; (b) at g/D =3.00 both at Re = 1500

B. Variation of the Coefficients of Drag and Lift

The two cylinders have individual coefficients of drag and lift at a particular spacing ratio. It is important to state that Cd and Cl behind the cylinders fluctuate with time.

Fig. 7 illustrates the time history of Cd at g/D =1.75. It shows that the fluctuation of coefficient of drag behind both the upper and the lower cylinders is

irregular. Similarly, Fig. 8 represents the irregular variation of Cl behind the two cylinders at the same g/D. At this small g/D, weaker biased and flip-flopping flow occurs. This accounts for the irregular fluctuation pattern.

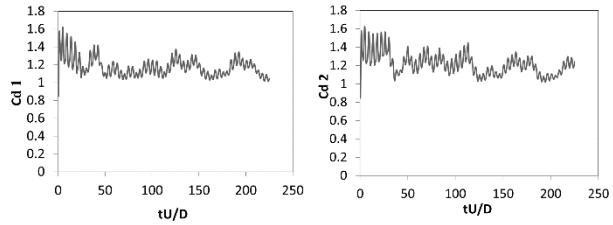

Fig. 7. Variation of Cd behind lower cylinder (a); Cd behind upper cylinder (b) at g/D =1.75. Subscripts on vertical axis: 1- lower cylinder; and 2- upper cylinder

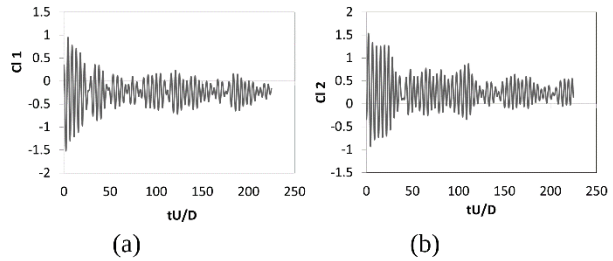

Fig. 8. Variation of Cl behind lower cylinder (a); Cl behind upper cylinder (b) at g/D = 1.75

Like g/D =1.75, a weak biased flip-flopping flow also exists at g/D = 2.00 [26], and is responsible for the irregular fluctuations of Cd and Cl (Fig. 9).

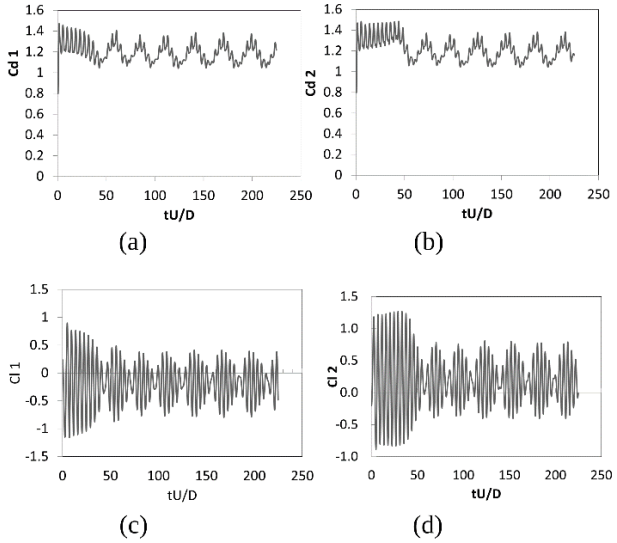

Fig. 9. Variation of Cd - a, b; Cl- c, d at g/D = 2.0.

On the other hand, at g/D ≥ 2.50, there is regular fluctuation of Cd behind the cylinders (Fig. 10). Fig. 10 (a and b) describes the regular variation of Cd at g/D = 2.50; Fig. 10 (c and d) illustrates how unsteadiness diminishes after the flow begins, so that Cd thereafter varies about a mean value with time, at g/D =3.50. Fig. 10 (e and f) also shows that after some time, Cd oscillates about a mean value, throughout the rest of the flow time at much higher g/D = 5.00.

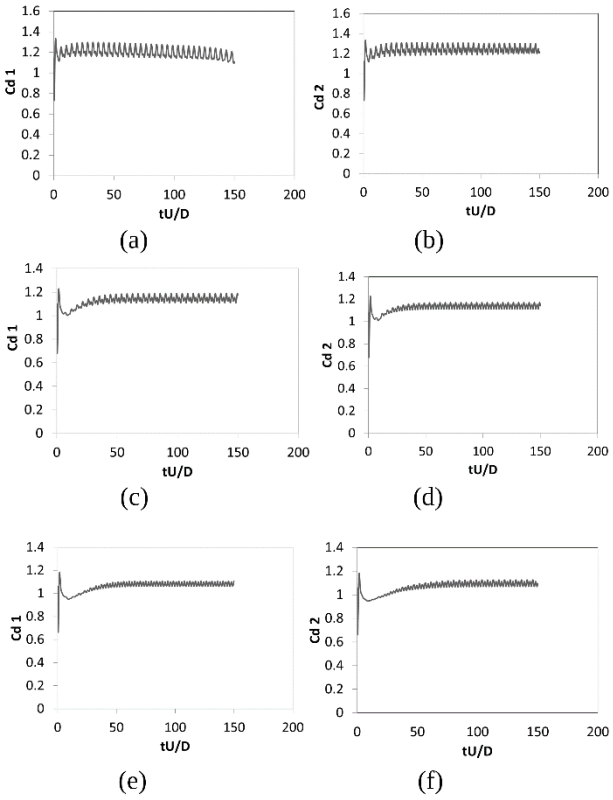

Fig. 10. Variation of Cd behind lower cylinder (1) and upper cylinder (2) - (a) and (b) are at g/D =2.5; (c) and (d) are at g/D = 3.5; and (e) and (f) are at g/D = 5.0.

Similarly, Fig. 11 illustrates the time history of Cl at g/D = 2.5, 3.5 and 5.0. Expectedly, biased flow does not take place above critical spacing ratios g/D > 2.0, so that Cl fluctuations behind the cylinders are of consistent pattern. Like the Cd fluctuation, Cl variation at g/D ≥ 2.5 is of increasingly vivid and regular pattern such that flow unsteadiness quickly diminishes and Cl oscillates about a mean value.

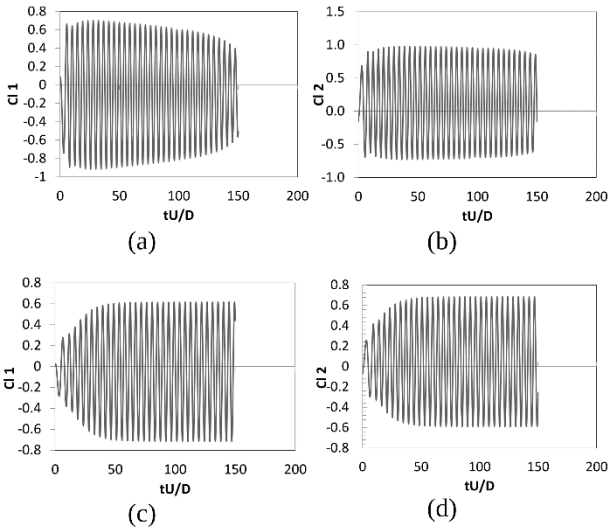

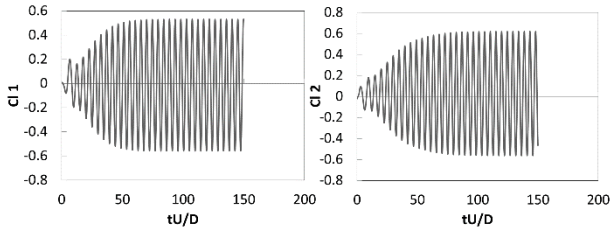

(e) (f)

Fig.11. Variation of Cl behind lower cylinder (1) and upper cylinder (2) – a and b are at g/D =2.5; c and d are at g/D = 3.5; and e and f are at g/D = 5.0

C. Relationship between Strouhal Number, Drag, Lift Coefficient and g/D

The mean and rms lift and drag coefficients were determined for the individual cylinders at the critical spacing ratios g/D. These mean and rms values represent single weighted values of the fluctuating lift and drag coefficients, respectively. Table IV presents the mean lift coefficient ($\bar{Cl}$) and mean drag coefficient ($\bar{Cd}$) of the lower cylinder (LC) and upper cylinder (UC). Table IV depicts that at g/D ≤ 2.00, the $\bar{Cl}$ for the upper cylinder is greater than that at the greater g/D. The reason ascribable to this is the phenomenon of biased flow due to small gaps, in which the vortices from the lower cylinder deflect more towards the upper cylinder or vice versa. This therefore increased the lift force coefficient for the upper cylinder, as earlier suggested by Lam et al [14]. It had previously been remarked that very small gap resulted in steep increase of lift coefficient [27].

Furthermore, Fig. 12 shows the relationship between mean force coefficients and the g/D. Fig. 12a depicts that the mean lift coefficients of the upper cylinder decrease as g/D increases, while those of the lower cylinder increases as g/D widens. On the other hand, Fig. 12b shows how the $\bar{Cd}$ for the upper cylinder increases from g/D = 1.75 to maximum at g/D = 2.50 and then continually decreases until g/D = 5.00. At around g/D = 3.45, $\bar{Cd}$ for both the upper and the lower cylinders are equal (mean Cd = 1.126). Thereafter, the mean Cd of the lower cylinder decreases as g/D ≥ 3.50.

TABLE IV. STROUHAL NUMBER AND $\bar{Cl}$ AND DRAG COEFFICIENTS AT RE = 1.5 X 10^3

g/D		$\bar{Cl}$	$\bar{Cd}$	St
1.75	LC	-0.232	1.174	0.238
	UC	0.244	1.213	0.238
2.00	LC	-0.168	1.193	0.211
	UC	0.176	1.216	0.243
2.50	LC	-0.0923	1.195	0.229
	UC	0.114	1.236	0.229
3.0	LC	-0.072	1.128	0.222
	UC	0.070	1.158	0.222
3.50	LC	-0.043	1.126	0.215
	UC	0.043	1.122	0.215
4.00	LC	-0.031	1.100	0.215
	UC	0.027	1.082	0.215
5.00	LC	-0.012	1.062	0.215
	UC	0.023	1.065	0.209

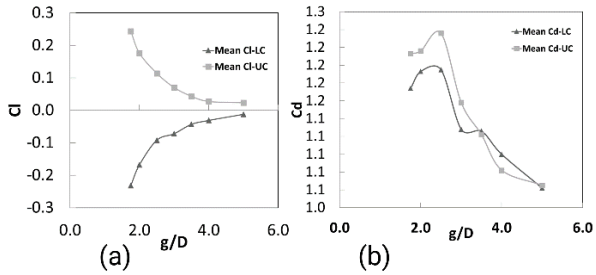

(a) (b)

Fig. 12. (a) Variation of the mean Cl with g/D; it shows that mean Cl of lower increases but upper cylinder decreases with g/D ratios. (b) Variation of mean Cd with g/D; intersection of the curves for upper cylinder and lower cylinder shows more intermediate g/D where the cylinders mean Cd are equal

The use of rms to evaluate the drag coefficient and lift coefficient annuls the negative signs due to fluctuations in addition to indicating time-averaged effects of these force coefficients. Table V presents the Cd_{rms} and Cl_{rms} of both the upper and lower cylinders. Further, Fig. 14 shows the relationship of the rms values with the g/D. The Cl_{rms} of the upper cylinder increases from 0.421 at g/D = 1.75 to a maximum of 0.586 at g/D = 2.50 (Fig. 13a). Then, Cl_{rms} decreases sharply at g/D = 3.00 and continues to decrease until g/D = 4.00 before it again increases at g/D = 5.00. The Cl_{rms} of the lower cylinder changes with g/D in a pattern resembling the upper cylinder. At g/D = 3.38, both cylinders have Cl_{rms} = 0.43, while at g/D = 4.8, $Cl_{rms} \approx 0.38$.

On the other hand, the Cd_{rms} of the upper cylinder also increased from g/D = 1.75 to a maximum value at g/D = 2.50 (Fig. 13b). Thereafter, it continues to

decrease up to g/D = 5.00. The lower cylinder reaches its maximum value of Cd_{rms} ≈ 1.2 at g/D = 2.25. Then, it declines until g/D = 5.0. At g/D = 3.4, both cylinders have Cd_{rms} ≈1.128, while at g/D = 4.82, Cd_{rms} ≈ 1.068. It is noted that Cd_{rms} and $\bar{Cd}$ both have the same pattern of variation with the g/D (Fig. 12b and 13b).

TABLE V. RMS LIFT AND DRAG COEFFICIENTS AT RE = 1.5 X 10^3

g/D		Cl_{rms}	Cd_{rms}
1.75	LC	0.381	1.178
	UC	0.421	1.218
2.00	LC	0.412	1.196
	UC	0.458	1.220
2.50	LC	0.520	1.196
	UC	0.587	1.237
3.00	LC	0.400	1.129
	UC	0.439	1.158
3.50	LC	0.441	1.127
	UC	0.426	1.122
4.00	LC	0.394	1.101
	UC	0.349	1.083
5.00	LC	0.346	1.062
	UC	0.362	1.066

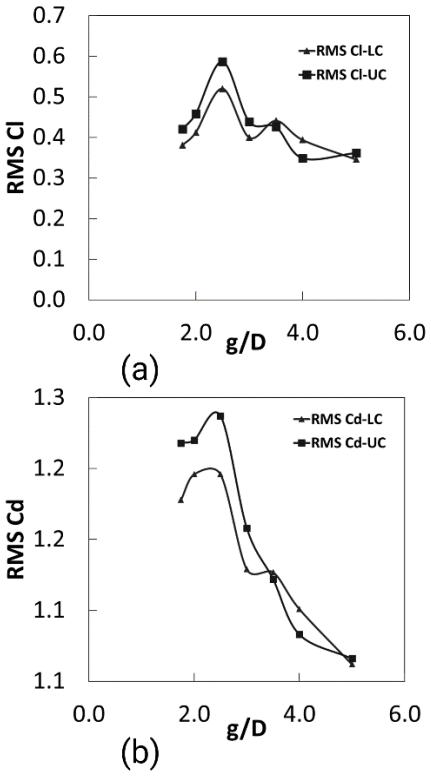

Fig. 13. The variation of rms Cl and rms Cd with the g/D. (a) two rms Cl for the two cylinders approach the same value around g/d =3.5; this is same for rms Cd in (b). While the table shows g/d where rms Cd and Cl of two cylinders are the same, the figure gives a pictorial illustration of the rise and fall of the Cd and Cl

From lift coefficient around the cylinders, Strouhal number was evaluated. Fig. 14 illustrates the variation of St with g/D. The St increases to a maximum as g/D decreases from 5.00 to 2.00 for the upper cylinder. At 3.50 ≤ g/D ≤4.00, St does not change. Like the mean lift coefficients, the St of the upper cylinder has highest values at g/D = 1.75 and 2.00. On the other hand, the St of the lower cylinder increases at g/D =5.00 up to g/D = 3.50, and then sharply increases to one maximum at g/D =2.50, at which point it is equal to the St of the upper cylinder. While the St of the upper cylinder reaches its peak at g/D =2.00, St of the lower cylinder reaches a minimum at this g/D.

Furthermore, the biased flow at g/D = 1.75 and 2.00 accounts for the reason why two peaks of power spectral density (PSD)- with one being significant- occur in PSD-St graph for both the upper and lower cylinders (Fig. 15). However, only a single peak of PSD occurs at g/D ≥2.50 for both cylinders (Fig. 16).

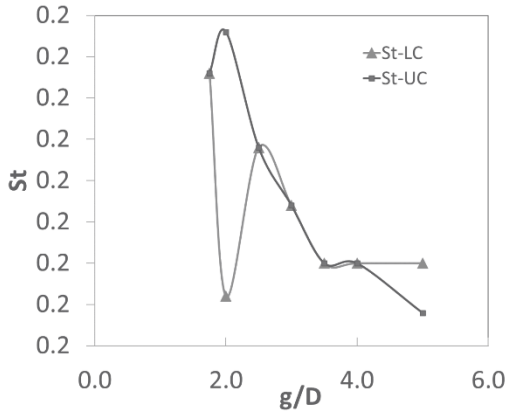

Fig. 14. Variation of Strouhal number with g/D. The interception shows spacing ratios at which frequency-measure of vortex shedding from the two cylinders are the same. St = Strouhal number

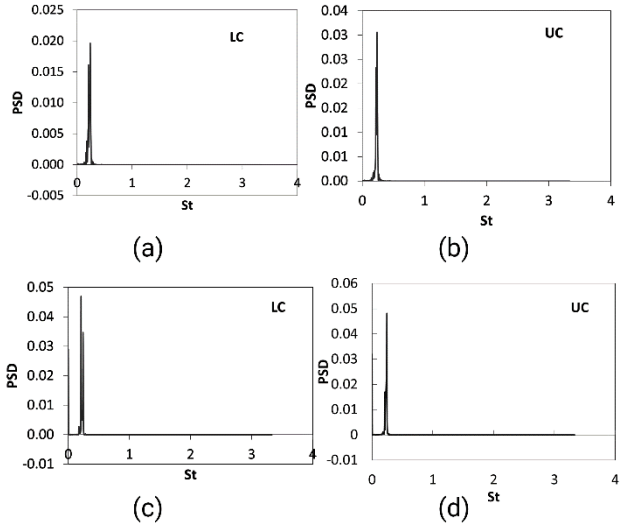

Fig. 15. PSD versus St with two peaks recorded: (a and b) at g/D = 1.75; (c and d) at g/D =2.0. Both a and b are at Re = 1500. Only a single peak is recorded at spacing ratios. PSD = power spectral density. Strouhal number is the dimensionless frequency parameter corresponding to the peak PSD.

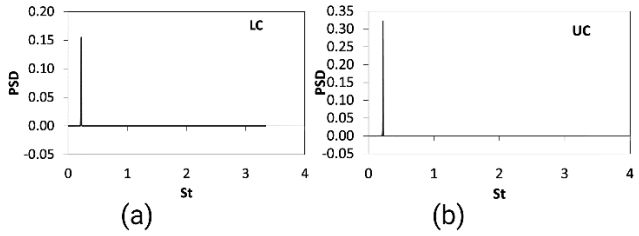

Fig. 16. PSD versus St with single peak: (a) lower cylinder; (b) upper cylinder, presented at Re = 1500, g/D = 3.0 g/D ≥ 2.5 gives only a single peak PSD.

VII. Discussion and Conclusion

It had been shown that the RNG k-ε preferably optimized the mean Cd, Cl and St compared with the standard and realizable k-ε models using a single cylinder at Re = 1000 and Re =3900. The RNG k-ε turbulence model was used to determine the Cd, Cl and St of two side-by-side circular cylinders in a viscous flow at Re = 1500. This model was thereafter adopted for Re = 1500 because it yielded Cd, Cl and St more accurate than those of standard k-ε and the realizable k-ε models when the three models were compared with the LES and experimental data [6, 21, 22] at Re = 1000 and Re =3900 for a single cylinder. In particular, the results presented by Wang were obtained using RNG k-ε model [6] via total variation diminishing scheme. The small gap ratios g/D = 1.75 and g/D =2.0 were significant and critical to the behaviour of all the fluid dynamic parameters investigated. At these spacing ratios, biased flow occurs, whereby the vortices shed from one of the two cylinders were deflected and inclined towards the other cylinder. This phenomenon had been reported previously in [14]. This consequently caused the irregular fluctuations of the Cd and Cl over the cylinders [26].

Similar to Lam et al [13], two peaks (one of which is distinct) of the power spectral density (PSD) were obtained at g/D ≤ 2.0, which is equivalent to biased flow. Since no biased flow took place, only a single peak of PSD is observed at g/D ≥ 2.5. The mean lift coefficient of the lower cylinder increased to a maximum as g/D decreased from 2.5 to g/D =1.75, consistent with the finding of [26]. Highest values of Strouhal number were recorded at g/D = 1.75 and g/D =2.0 respectively for the lower and upper cylinders. Flow interference was very strong at these spacing ratios. As g/D increased gradually from 3.0 to 5.0, the flow interference greatly reduced [26].

Though results of this work demonstrated that RNG k-ε turbulence model can predict the hydrodynamic force coefficients better than the other two k-ε turbulence models for cylinder flow, there are some limitations to highlight. The convergence criteria set for all simulations was 10^{-3}. Although this is large compared to 10^{-6} used in [26], it enabled us to attain solution convergence with results, which compared well with data from the literature, within 2-4 hours. 10^{-6} convergence criterion was not used because the simulation at this criterion took several hours to converge. Moreover, only two-dimensional transient planar flow was considered. Including the third dimension can affect the results to some degree. 3D effect becomes significant at the critical spacing ratios when height-to-diameter ratio of the cylinder = 16 so that results obtained in three-dimensional flow over cylinder show discrepancy as compared to two-dimensional flow [28].

Consequently, under two-dimensional consideration or assumption that the height-to-diameter is below a certain value [28], these 3D effects are insignificant. The two-dimensional consideration provides some insights into the accuracies of these three turbulence models. Therefore, RNG k-ε is potentially a preferred k-ε turbulence model for optimization of flow-induced vibration involving a bank of cylinders or tubes in heat exchangers, and chimney stack, so as to minimize structural damage arising from vibration.

REFERENCES

[1] Oyewola, O.M., et al., Numerical Simulation Of Forced Convective Flows Over A Pair Of Side-By-Side Heated Circular Cylinders. ARPN Journal of Engineering and Applied Sciences, 2021. 16(13): p. 1312-1322.

[2] Oyewola, O.M., O.S. Ismail, and K. Abu, Numerical Simulation of Forced Convection Flows over a Pair of Circular Cylinders in Tandem Arrangement. Jordan Journal of Mechanical and Industrial Engineering, 2019. 13(4): p. 221-230.

[3] Orszag, S.A., et al., Renormalization-Group Modeling and Turbulence Simulations. Near-Wall Turbulent Flows, 1993: p. 1031-1046.

[4] Shih, T.-H., et al., A new k-ϵ eddy viscosity model for high reynolds number turbulent flows. Computers & Fluids, 1995. 24(3): p. 227-238.

[5] Wang, J.-s. and Z. Huang, A TVD Scheme for Incompressible Flow Coupled With Different Turbulence Modles on A Ground-Mounted Square-RIB Flow. Journal of Hydrodynamics, Ser. B, 2007. 19(6): p. 743-750.

[6] Wang, J.S., Flow around a Circular Cylinder Using a Finite-Volume Tvd Scheme Based on a Vector Transformation Approach. Journal of Hydrodynamics, 2010. 22(2): p. 221-228.

[7] Xu, F.Y., X.Y. Ying, and Z. Zhang, Prediction of unsteady flow around a square cylinder using RANS. Advances in Mechanical Engineering, Pts 1-3, 2011. 52-54: p. 1165-1170.

[8] Soe, T.M. and S.Y. Khaing. Comparison of Turbulence Models for Computational Fluid Dynamics Simulation of Wind Flow on Cluster of Buildings in Mandalay. 2017.

[9] Zhang, D., Comparison of Various Turbulence Models for Unsteady Flow around a Finite Circular Cylinder at Re=20000. Journal of Physics: Conference Series, 2017. 910: p. 012027.

[10] Pang, A.L.J., M. Skote, and S.Y. Lim, Turbulence Modeling Around Extremely Large Cylindrical Bluff Bodies, in The Twenty-third International Offshore and Polar Engineering Conference. 2013. p. ISOPE-I-13-162.

[11] James, W.D., S.W. Paris, and G.N. Malcolm, Study of Viscous Crossflow Effects on Circular Cylinders at High Reynolds Numbers. AIAA Journal, 1980. 18(9): p. 1066-1072.

[12] ANSYS, I., ANSYS FLUENT 12.0 Theory Guide. 2009.

[13] Versteeg, H.K. and W. Malalasekera, An introduction to computational fluid dynamics : the finite volume method. 2nd ed. 2007, Harlow, England ; New York: Pearson Education Ltd. xii, 503 p.

[14] Lam, K., J.Y. Li, and R.M.C. So, Force coefficients and Strouhal numbers of four cylinders in cross flow. Journal of Fluids and Structures, 2003. 18(3-4): p. 305-324.

[15] West, G.S. and C.J. Apelt, Fluctuating lift and drag forces on finite lengths of a circular cylinder in the subcritical Reynolds number range. Journal of Fluids and Structures, 1997. 11(2): p. 135-158.

[16] Launder, B.E. and D.B. Spalding, The numerical computation of turbulent flows. Computer Methods in Applied Mechanics and Engineering, 1974. 3(2): p. 269-289.

[17] Lima E Silva, A.L.F., A. Silveira-Neto, and J.J.R. Damasceno, Numerical simulation of two-dimensional flows over a circular cylinder using the immersed boundary method. Journal of Computational Physics, 2003. 189(2): p. 351-370.

[18] Park, J., K. Kwon, and H. Choi, Numerical solutions of flow past a circular cylinder at Reynolds numbers up to 160. Ksme International Journal, 1998. 12(6): p. 1200-1205.

[19] Sucker, D. and H. Brauer, Fluiddynamik bei quer angeströmten Zylindern. Wärme - und Stoffübertragung, 1975. 8: p. 149-158.

[20] Labbe, D.F.L. and P.A. Wilson, A numerical investigation of the effects of the spanwise length on the 3-D wake of a circular cylinder. Journal of Fluids and Structures, 2007. 23(8): p. 1168-1188.

[21] Huang, Y.-q., J. Deng, and A.-l. Ren, Research on lift and drag in unsteady viscous flow around circular cylinders. Journal-Zhejiang University Engineering Science, 2003. 37: p. 596-601.

[22] Roshko, A., Experiments on the flow past a circular cylinder at very high Reynolds number. Journal of Fluid Mechanics, 1961. 10(3): p. 345-356.

[23] Kravchenko, A.G. and P. Moin, Numerical studies of flow over a circular cylinder at ReD=3900. Physics of Fluids, 2000. 12(2): p. 403-417.

[24] Jia, X.H. and H. Liu, Large eddy simulation of flow around two circular cylinders. Chinese Journal of Hydrodynamics, 2008. 23: p. 625-632.

[25] Norberg, C., Fluctuating lift on a circular cylinder: review and new measurements. Journal of Fluids and Structures, 2003. 17(1): p. 57-96.

[26] Sarvghad-Moghaddam, H., N. Nooredin, and B. Ghadiri-Dehkordi, Numerical simulation of flow over two side-by-side circular cylinders. Journal of Hydrodynamics, Ser. B, 2011. 23(6): p. 792-805.

[27] Zdravkovich, M.M., Forces on a circular cylinder near a plane wall. Applied Ocean Research, 1985. 7(4): p. 197-201.

[28] Lam, K., W.Q. Gong, and R.M.C. So, Numerical simulation of cross-flow around four cylinders in an in-line square configuration. Journal of Fluids and Structures, 2008. 24(1): p. 34-57.